Journal of Zhejiang University-SCIENCE A (Applied Physics & Engineering) 2025 26(3):252-265
www.jzus.zju.edu.cn; www.springer.com/journal/11582
E-mail: jzus_a@zju.edu.cn

Research Article

https://doi.org/10.1631/jzus.A2400292

Enhancing the spatter-removal rate in laser powder-bed fusion using a gas-intake system with dual inlets

Xin TIAN[1], Junwei ZHONG[1]✉, Youwen YANG[1,2]✉, Chaolei ZHANG[1], Long ZHAO[1]

[1]*School of Mechanical and Electrical Engineering, Jiangxi University of Science and Technology, Ganzhou 341000, China*
[2]*College of Engineering and Applied Science, Nanjing University, Nanjing 210089, China*

Abstract: Mounds of spatter are generated in laser powder-bed fusion (L-PBF) additive manufacturing, which reduces build quality and laser lifetime. Due to the lack of supplemental airflow above the chamber, the conventional build chamber with a single gas inlet exhibits a pronounced tendency for gas to flow upward near the outlet. This phenomenon results in the formation of a large vortex within the build chamber. The vortex leads to the chaotic motion trajectory of the spatter in the build chamber. The design defects of the existing build chamber based on dual gas inlets are shown in this paper. We established a coupled computational fluid dynamics-discrete phase model (CFD-DPM) model to optimize the build chamber by adjusting the position and structure of the second gas inlet. The homogeneity of the flow is increased with a distance of 379 mm between the two inlets and a wider-reaching second inlet. The Coanda effect is also crucial in the spatter-removal process. The Coanda effect is reduced by modifying the right sidewall of the build chamber and increasing the pressure difference between the inlet and outlet. Finally, we found that the spatter-removal rate rose from 8.9% to 76.1% between the conventional build chamber with a single gas inlet and the optimized build chamber with two gas inlets.

Key words: Laser powder-bed fusion (L-PBF); Computational fluid dynamics (CFD); Flow field simulation; Structural optimization; Coanda effect

1 Introduction

Laser powder-bed fusion (L-PBF) technology offers higher build accuracy and surface quality than other metal additive manufacturing technologies. With fast manufacturing, low cost, and the ability to print parts with complex geometrics, it is widely used in the production of complex components such as automotive, aerospace, defense parts, medical devices, and consumer products (Amiri and Payton, 2021; Debroy et al., 2021; Jadhav and Jadhav, 2022; Dong et al., 2024). However, in the L-PBF process, the metal powder forms a molten pool when the temperature attains the melting point under the action of a high-energy laser; then the powder vaporizes to form metal vapor when the surface temperature of the molten pool exceeds the boiling point, which is harmful to the part-building process. For example, the spatter entrains and settles to merge with the melt pool and is one of the source materials for the final weld bead produced by L-PBF. In addition, when the temperature of the melt pool falls, these particles remain incompletely melted and become a source of roughness and porosity in the printed parts (Yadroitsev et al., 2010; Matthews et al., 2016). The spatter absorbs and attenuates the laser energy, which makes the sintering energy lower than the set value. The spatter also causes scattering, leading to laser-focus shift and poor manufacturing accuracy (Greses et al., 2004; Shcheglov et al., 2013). Therefore, the removal of this spatter is of paramount importance in avoiding defective parts.

Extensive research has been done to reveal the generation mechanism of spatter. Scientists have observed the dynamic spattering process of cobalt-chromium alloys during L-PBF with a high-speed video camera (Wang et al., 2017). The characteristics and formation mechanism of the spatter were revealed by in

✉ Junwei ZHONG, jwzhong0@jxust.edu.cn
Youwen YANG, yangyouwen@jxust.edu.cn
Junwei ZHONG, https://orcid.org/0000-0003-0277-3747
Youwen YANG, https://orcid.org/0000-0003-1557-0252

Received June 7, 2024; Revision accepted Aug. 2, 2024;
Crosschecked Feb. 20, 2025

situ high-speed, high-energy X-ray imaging that allowed the team to quantify the velocity, size, and direction of the spatter (Young et al., 2020). The dynamic behavior of the spatter-generation process was also investigated using a high-speed camera technique (Gunenthiram et al., 2018). Various strategies have been proposed to minimize the impact of spatter on L-PBF part quality. In terms of laser volumetric energy density, Andani et al. (2018) found that increasing the laser scanning speed or decreasing laser power could reduce spatter, using image analysis techniques. The advantage of this strategy is that a higher scanning velocity and lower laser power can reduce the amount of hot spatter. However, higher scanning velocity results in a longer scanning path, which increases the cold spatter caused by entrainment. Furthermore, higher scanning velocity and lower laser power can keep the temperature of the melt pool from reaching the level required. Incomplete melting of powder particles results in structural defects. In terms of the scanning path, relevant research shows that consistency between the laser-scanning direction and spatter-removal airflow can significantly reduce spatter accumulation near the chamber outlet, but that thickly accumulated spatter is still difficult to remove (Bin Anwar and Pham, 2017, 2018). The transient dynamics of the spatter during L-PBF vary with time, ambient pressure, and position, and the overall amount of the spatter decreases as the ambient pressure increases (Guo et al., 2018). Vacuum conditions and high laser-scanning speed are detrimental to powder-bed stability, which leads to more spatter (Annovazzi et al., 2022). Other factors that affect spatter generation are protective gas composition (Pauzon et al., 2021), laser mode (volume energy density (VED)) (Nguyen et al., 2020; Sow et al., 2020), laser pre-sintering (Constantin et al., 2021; Annovazzi et al., 2022), and powder material (Tan et al., 2017; Gunenthiram et al., 2018).

The studies described above attempted to reduce the impact of spatter beginning with spatter generation. However, the requirements of the L-PBF process make it difficult to reduce the impact of reducing spatter further. The gas-flow strategy is another effective way to improve spatter removal in practice. It enables an undisturbed process by using gas flow to remove spatter from the process zone. Numerical simulation techniques have been widely used to study the complex flow of spatter motion during the L-PBF process. Chien et al. (2021) proposed a coupled computational fluid dynamics-discrete phase model (CFD-DPM) simulation framework to optimize the flow field of the protective gas in L-PBF. Wang et al. (2022) numerically simulated the interaction between the protective gas flow and the spatter by building a full-size model of the build chamber. Another group developed a CFD model to simulate the homogeneity of the protective gas flow in the build chamber, which affects the values and ranges of the compressive strength and density of the constructed part (Ferrar et al., 2012). A more uniform flow was achieved by redesigning the gas-delivery pipe. Gao et al. (2023) also tried to reorganize the protective gas flow by optimizing the structure of the L-PBF build chamber. They used a combination of numerical simulations and experiments to optimize the wind-field circulation structure of the chamber, which resulted in a parabolic wind-field circulation trajectory (Gao et al., 2023). The wind-field circulation structure was optimized by increasing the number of nozzles in the main air duct. Meanwhile, Zhang et al. (2020) used a design based on the inverse Coanda effect to improve the spatter-removal rate.

In summary, most studies have concentrated on factors such as spatter jet velocity, angular dispersion, and spatter redeposition sites. Different strategies have been proposed to reduce spatter generation. In contrast, research on the gas-flow strategy focuses on the interaction between the flow field and the spatter. The gas-flow strategy operates in the build chamber using a combination of a single gas inlet and a single gas outlet. However, the key factor that determines the homogeneity of the flow above the powder bed has not been thoroughly explored. What is clear is that the gas supplied by a single inlet tends to flow upward near the outlet due to the lack of additional gas supplied on the upside of the build chamber. The nose-up of the flow near the outlet destroys the homogeneity of the flow above the powder bed and impedes spatter removal.

Our first step here will be to examine the design defects of the existing build chamber based on dual gas inlets. The aim of this study was to propose a design solution for a novel build chamber that would enhance the spatter-removal rate for L-PBF technology. We established a fully coupled CFD-DPM to model the flow pattern and particle trajectory. Based on the homogeneity of the flow, the threshold velocity, and

the removal rate of particles, we assessed the proposed spatter-removal gas-flow system.

2 Numerical simulation method

The effectiveness of spatter removal mainly depends on the drag force of the protective gas flow and the gravitational forces. We built a fully coupled CFD-DPM model to simulate the complex flow involving the protective gas and spatter in an L-PBF chamber.

2.1 Theoretical foundations

The gas flow in the L-PBF chamber was simulated using ANSYS FLUENT software and the *k*-*ε* turbulence model. The continuity and momentum equations can be expressed as follows:

$$\rho\nabla\cdot V=0, \tag{1}$$

$$\begin{aligned}\nabla\cdot(\rho uV)&=-\frac{\partial p}{\partial x}+\frac{\partial\tau_{xy}}{\partial x}+\frac{\partial\tau_{yx}}{\partial y}+\frac{\partial\tau_{zx}}{\partial z}+\rho f_x,\\ \nabla\cdot(\rho vV)&=-\frac{\partial p}{\partial y}+\frac{\partial\tau_{xy}}{\partial x}+\frac{\partial\tau_{yy}}{\partial y}+\frac{\partial\tau_{zy}}{\partial z}+\rho f_y,\\ \nabla\cdot(\rho\omega V)&=-\frac{\partial p}{\partial z}+\frac{\partial\tau_{xz}}{\partial x}+\frac{\partial\tau_{yz}}{\partial y}+\frac{\partial\tau_{zz}}{\partial z}+\rho f_z,\end{aligned} \tag{2}$$

where ∇V is the time rate of change of the relative change in volume per unit volume of a fluid microcluster in motion; ρ is the fluid density; p is the static pressure; $\boldsymbol{\tau}$ is the stress tensor; f is the external force; u, v, and ω are velocity components in x, y, and z directions.

The transport equation of the *K*-*ε* turbulence model can be expressed as follows:

$$\begin{aligned}&\frac{\partial(\rho K)}{\partial t}+\frac{\partial(\rho\overline{u}_jK)}{\partial x_j}=\frac{\partial}{\partial x_j}\left[\left(\mu+\frac{\mu_t}{P_{\gamma K}}\right)\frac{\partial K}{\partial x_j}\right]+\\ &G_K+G_b-\rho\varepsilon-Y_M+S_K,\end{aligned} \tag{3}$$

$$\begin{aligned}&\frac{\partial\rho\varepsilon}{\delta t}+\frac{\partial(\rho\overline{u}_j\varepsilon)}{\partial x_j}=\frac{\partial}{\partial x_j}\left[\left(\mu+\frac{\mu_t}{P_{\gamma K}}\right)\frac{\partial\varepsilon}{\partial x_j}\right]+\\ &C_{\varepsilon1}\frac{\varepsilon}{K}(G_K+C_{\varepsilon3}G_b)-C_{\varepsilon2}\rho\frac{\varepsilon^2}{K}+S_\varepsilon,\end{aligned} \tag{4}$$

where K and ε are the turbulent kinetic energy dissipation rates; μ is the dynamic viscosity; u_j is the velocity component; μ_t is the vortex viscosity; G_k is the turbulent kinetic energy due to the mean velocity gradient; G_b is the generating term of the turbulent kinetic energy K due to buoyancy, which is an incompressible fluid in the present study, therefore, G_b=0; $\rho\varepsilon$ is the dissipation term; Y_M is the compressibility correction term, which is the contribution of pulsatile expansion in the compressible turbulence; S_K and S_ε are the source terms for the equations K and ε, respectively. The constants take the values: $C_{\varepsilon1}$=1.44, $C_{\varepsilon2}$=1.92, $C_{\varepsilon3}$=0, and $P_{\gamma K}$=1.0.

An important indicator for optimizing the flow structure of the build chamber for spatter removal is whether the particles are "blown" out of the chamber. Thus, it was crucial to accurately simulate the spatter trajectories. We used the discrete phase model to trace the trajectories. A fully coupled CFD-DPM model was constructed to study the interaction between the gas flow and the spatter. The integrated fluid-particle pressure and momentum equations were treated with the semi-implicit method for pressure linked equations (SIMPLE) algorithm.

The jumping of the particles on the surface of the powder bed was another issue that required particular focus when optimizing the flow structure of the build chamber. During the L-PBF manufacturing process, the high-speed gas flow can induce movement of the particles on the surface of the powder bed, which will lead to localized uneven powder-layer thickness and ultimately affect part quality. Therefore, the local flow velocity should be strictly limited. Fig. 1 illustrates the force analysis of the particles on the surface of the powder bed. A jump will occur if the wind stress given by the gas flow causes the surface particles to rotate around their neighboring support point (point *c* in Fig. 1). The jump occurs when the moments of the aerodynamic drag (F_d) and aerodynamic

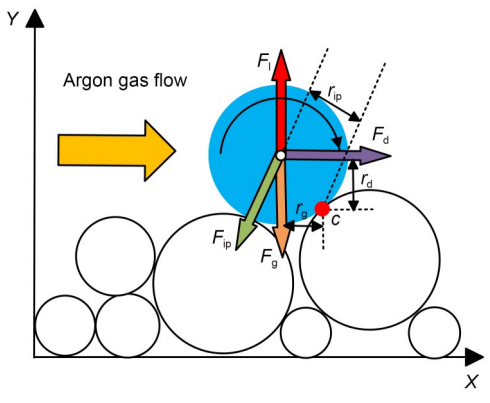

Fig. 1 Schematic diagram of moment balance of a particle

lift (F_l) exceed the moments of interparticle cohesion (F_{ip}) and gravity (F_g) (Kok et al., 2012). The moment balance equation is as follows:

$$r_d F_d \approx r_g (F_g - F_l) + r_{ip} F_{ip}, \tag{5}$$

where r_d, r_g, and r_{ip} are proportional to the particle diameter d, and F_d, F_g, F_l, and F_{ip} are the drag, gravity, lift, and cohesion, respectively.

2.2 Physical description of the simulation study

We propose a novel gas-intake system with dual gas inlets for spatter removal from the build chamber, as shown in Fig. 2a. A second gas inlet is added above the main gas inlet compared with the conventional build chamber. The center of the powder-bed surface is set as the coordinate origin, the horizontal direction of the main gas inlet is the Z direction, and the vertical direction from the powder bed to the laser mirror chamber is the Y direction. The size of the powder bed is 460 mm×370 mm in the X and Y directions. The main gas inlet consists of 300 cylindrical nozzles with 6 rows and 50 columns, and the size of the inlet is 514 mm×42 mm in the X and Y directions. The second gas inlet consists of 75 cylindrical nozzles with 3 rows and 25 columns, and the size of the inlet is 250 mm×13 mm in the X and Y directions. The distance between the centers of the two gas inlets is 454 mm. The center of the main gas inlet is 5 mm from the bottom of the powder bed in the Y direction. The size of the outlet is 600 mm×75 mm in the X and Y directions. The initial design of the second gas inlet had a width of 250 mm in the X direction.

As shown in Fig. 2b, the protective gas is blown into the build chamber from the gas-intake system, and brings the spatter towards the outlet. The exhausted protective gas is extracted by an exhaust fan to dedust in a filtering apparatus. The filtered protective gas is then reintroduced into the chamber.

2.3 Numerical settings

The trajectories of the dispersed particles are predominantly determined by the resistance of the gas flow (Bin Anwar et al., 2019). The dilute flow mechanism is considered for the interaction simulation of spatter and gas flow. In this type of flow, the interactions between the particles can be disregarded. Therefore, the particle-particle interaction was not considered in the flow simulation. Any particles that fall back into the powder bed, whether they continue to move or are deposited, will potentially affect the quality of the manufactured part. In the model, all particles that fell back into the powder bed

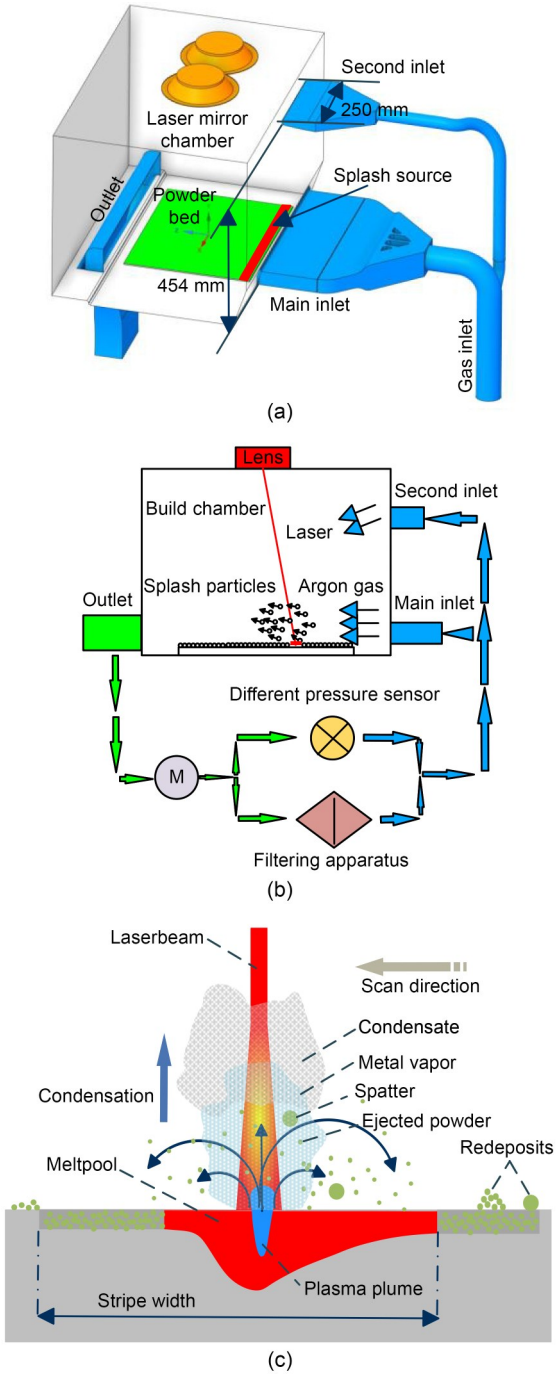

Fig. 2 Schematic of the build chamber with dual gas inlets: (a) 3D model of the build chamber; (b) circulatory system of the protective gas; (c) sputtering and other by-product generation

were defined as redeposited particles. The boundary-condition type of the powder bed was set as a "trap" to model the spatter deposition. The discrete phase-boundary condition type of the rest wall was set as "reflect". The discrete phase-boundary condition type of the inlet and outlet was set as "escape". The initial pressure was set to 101325 Pa, and the gravitational acceleration was taken as −9.81 m/s^2 in the Y direction. The inlet and outlet were set as the pressure inlet and pressure outlet, respectively. The pressure values were set as 5 Pa (the corresponding flow rate is 1080.9 L/min) and −15 Pa at the inlet and outlet, respectively, according to the actual situation. The detailed settings of the boundary conditions are shown in Table 1 and the material properties are listed in Table 2.

Table 1 Boundary-condition settings

Name	Boundary condition
Inlet	Pressure inlet
Outlet	Pressure outlet
Powder bed	"Trap" wall
Room wall	"Reflect" wall

Table 2 Material properties

Material	Phase	Density (kg/m^3)	Dynamic viscosity (Pa·s)
Argon	Continuous	1.6228	2.125×10^{-5}
316L	Discrete	7950	–

As shown in Fig. 2c, the primary source of spatter in L-PBF is the vaporization of metal powder. The powder forms a molten pool under the action of a high-energy laser, and then vaporizes as the temperature of the melt pool exceeds the boiling point. In the building area of the build chamber, the spatter is sputtered at a certain angle and speed at the laser irradiation position during the sintering process (Ladewig et al., 2016). According to the results of previous studies, the closer the particle-ejection position is to the air inlet, the more difficult it is to blow particles away from the build chamber. Therefore, the particle-spatter source was placed above the powder bed at a distance of 40 mm away from the gas inlet, as shown in Fig. 2a. The spatters were set to be spherical, as recommended (Simonelli et al., 2015). The diameter of the particles was between 10 and 100 μm, and speeds were between 1.5 and 35.0 m/s. Moreover, the particles were incident in a conical shape, with a cone angle in the range of 45° to 70°. We tracked the trajectories of the particles to assess the influence of flow patterns of protective gas on spatter-removal rate. Random spatter incidence angles were used in this study.

It was imperative to investigate the threshold velocity for particles jumping in the powder bed. Research indicates that the phenomenon of powder-bed particle jumping can be likened to the jumping behavior of sand particles in wind-driven sand transport. Eq. (6) provides a method of calculating the threshold velocity (u_*) for the metal particles (Shao and Lu, 2000).

$$u_* = \sqrt{A_{\mathrm{N}}\left(\delta_{\mathrm{p}} g d + \frac{\gamma}{\rho d}\right)}, \tag{6}$$

where A_{N} and γ are constants with values of 0.0123 and 0.0003 kg/s^2, respectively; g is the acceleration of gravity; ρ is the density of the protective argon gas used to remove the spatter; d is the diameter of the powder-bed particles; δ_{p} is the ratio of particle density to gas-flow density.

The threshold velocity of particles with diameters ranging from 10 to 200 μm was based on Eq. (6) (Zhang et al., 2020). Zhang et al. (2020) proposed that the minimum threshold velocity of gas flow for particles jumping on the surface of the powder bed should be 10.27 m/s (for particles with a diameter of 60 μm). We determined the threshold velocity at 1 mm above the powder bed to be 3.38 m/s. This velocity was crucial for accurately measuring the data and was derived from the logarithmic law profile equation. The equation that governs this relationship is:

$$\frac{u(z)}{u_*} = \frac{\left[\ln\left(\frac{z u_*}{\mu}\right)\right]}{k} + B, \tag{7}$$

where k is the "von Karmen" constant (takes 0.4). B is an additive constant derived from integrating the logarithmic velocity profile, with empirical estimates ranging from 4.9 to 5.1; here, B=5. z is the distance between the surface of the powder bed and the monitoring plane, and μ is the dynamic viscosity of the protective argon gas.

2.4 Mesh independence study

Mesh is one of the most important factors affecting the solution accuracy of numerical simulation. The maximum flow velocity of the wind field at 1, 5,

10, and 50 mm above the powder bed was extracted to evaluate the mesh independence. The mesh quantity was then refined by changing the mesh size of key areas such as the inlet and outlet pipes, inlet and outlet parts, laser chamber, and powder bed. Fig. 3 shows that the velocity became stable as the mesh number reached 7.5 million. We chose mesh with a grid of 9 million.

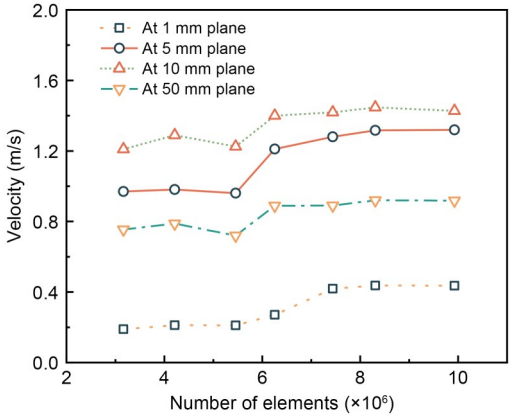

Fig. 3 Grid independence study

3 Result analysis and optimization

We used a quantitative assessment of spatter-removal rate, named removal rate, to evaluate the gas-intake system. The removal rate is defined as the number of removed spatters divided by the total number of generated spatters. The mathematical expression of removal rate (R_r) is:

$$R_r = \left(\frac{p_a - p_d}{p_a}\right) \times 100\%, \tag{8}$$

where p_d is the number of redeposited particles on the powder bed and p_a is the total number of generated spatters.

Furthermore, to provide a quantitative assessment of the consistency of gas-flow velocity near the powder bed, we introduced the concept of homogeneity as a measure of the dispersion of gas-flow-velocity distribution in the proximity of the powder bed. The term homogeneity (H) can be mathematically expressed as:

$$H = \left[1 - \left|\frac{v_{max} - v_{min}}{100 \times \overline{v_a}}\right|\right] \times 100\%, \tag{9}$$

where v_{max}, v_{min}, and $\overline{v_a}$ are the maximum, minimum, and average flow rates of gas on the monitoring plane, respectively.

The interaction between gas and spatter within the build chamber is depicted in Fig. 4. The number of spatters generated in the study was 1520. The number of redeposited spatters was 1389 for the original gas-intake system, resulting in a removal rate of 8.9%.

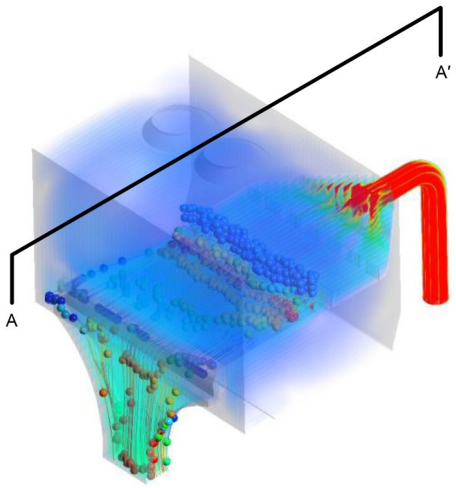

Fig. 4 Schematic diagram of simulated gas-spatter interaction for the initial design (the inlet pressure is 5 Pa). Different particle colors represent different particle speeds. The position of the result presentation plane is denoted as A–A′. The spatter-particle size is not accurately represented and the diagram does not encompass all possible spatter trajectories. References to color refer to the online version of this article

3.1 Effect of the second gas inlet

Ladewig et al. (2016) investigated the impact of homogeneity and velocity of protective gas flow on spattering during the L-PBF process. The results indicated that reducing the velocity of spatter-removal gas flow led to a decrease in spatter-removal rate. Several crucial design considerations for optimizing the airflow pattern were recommended by the group: (1) ensuring homogeneity of gas flow above the powder bed, (2) maximizing gas-flow rate to prevent by-product redeposition, (3) positioning the gas flow as close to the powder-bed surface as feasible, and (4) minimizing flow and turbulence of gas away from the powder bed and in the upward direction. Fig. 5 shows a comparison of the velocity contour between the build chamber with the original gas-intake system versus the new gas-intake system. In the build chamber with

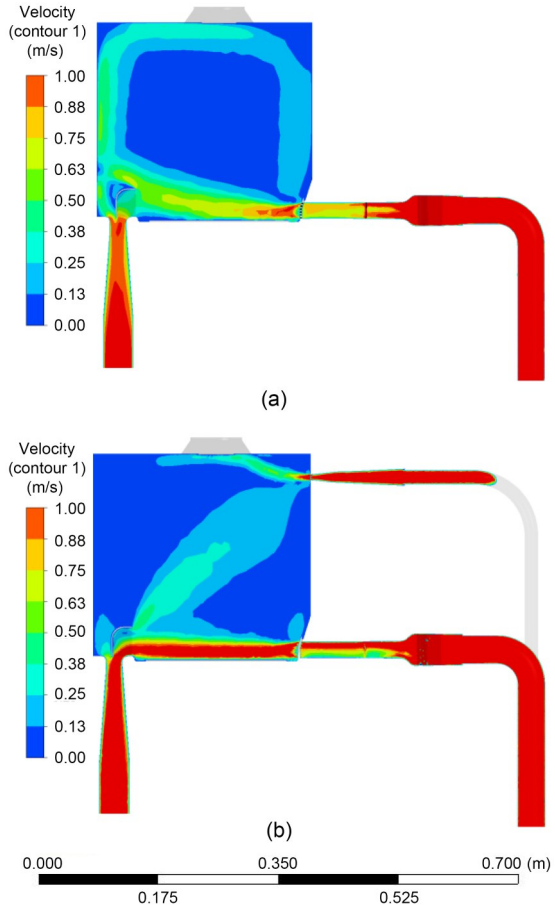

Fig. 5 Velocity contour on the middle slice in the *X* direction of the build chamber: (a) original gas-intake system (A–A′ plane); (b) new gas-intake system with a second inlet (A–A′ plane)

the original intake system, a clockwise-rotating vortex occupies almost the entire space. This flow pattern results in the formation of "laminar flow" around the powder bed. However, the protective gas from the inlet flows upward and slows down as it passes through the powder bed to the outlet. In the build chamber with the new intake system, the protective gas supplied by the second inlet suppresses the nose-up of the laminar flow from the main inlet. The protective gas from the main inlet becomes nearly parallel to the powder bed and flows directly to the outlet. The homogeneity and velocity of the "laminar flow" passing the powder bed were clearly increased, which provided uniform drag to the spatter. The removal rate from the build chamber with the new intake system increased to 24.1%. On the other hand, the presence of spatter in the laser path caused beam scattering, which leads to inefficient use of laser energy (Ferrar et al., 2012). The gas flow between the second inlet and the outlet provided a protective airflow over the laser path.

3.2 Optimization of the second gas inlet

As shown in Fig. 2a, in the initial design of the second gas inlet it was positioned 454 mm above the main gas inlet. We investigated the effect of the distance between the two inlets on the removal rate. Fig. 6 presents a velocity contour (with a streamline superposed on it) on the middle slice of the build chambers at different distances. We compared five distances: 354, 379, 429, 454, and 479 mm.

As shown in Fig. 6, the location of the vortex core next to the powder bed varied for different distances. When the distance between the two air inlets was less than 379 mm or more than 454 mm, the effect of the protective gas supplied by the second inlet on the laminar flow was reduced. Reverse flow was observed above the laminar flow near the outlet. The reverse flow was detrimental to the acceleration of the laminar flow. We studied the effect of the second airstream within the range of 379 to 454 mm. The detailed observations for different distances are discussed in the following paragraphs. We evaluated the effect of fluid drag force exerted by the airflow on particles by tracking particles with a diameter of 30 μm and speed of 4.5 m/s. Additionally, we conducted a statistical analysis to assess the removal efficiency of all particles.

(1) For the distance of 454 mm, the clockwise rotating vortex of the build chamber with the original gas-intake system was replaced by a series of counter-rotating vortex pairs. The main vortex pairs were split by the nose-up flow of the laminar flow from the main inlet. The protective gas flowed up to the second inlet due to the pressure differential between the two inlets. A clockwise rotating vortex then formed just above the powder bed. The spattering was highly affected by the downwash flow on the right of the clockwise-rotating vortex above the powder bed. The downwash flow moved to the particle incidence position with an obtuse angle of θ, which exerted horizontal and vertical drag forces on the spatter. The trajectories of the spatter with a diameter of 30 μm show that the maximum spatter distance in the horizontal direction was 140.6 mm and the average distance was 78.6 mm. The maximum spatter height in the vertical direction was 45.9 mm. The spatter-removal rate was 24.1% for this distance.

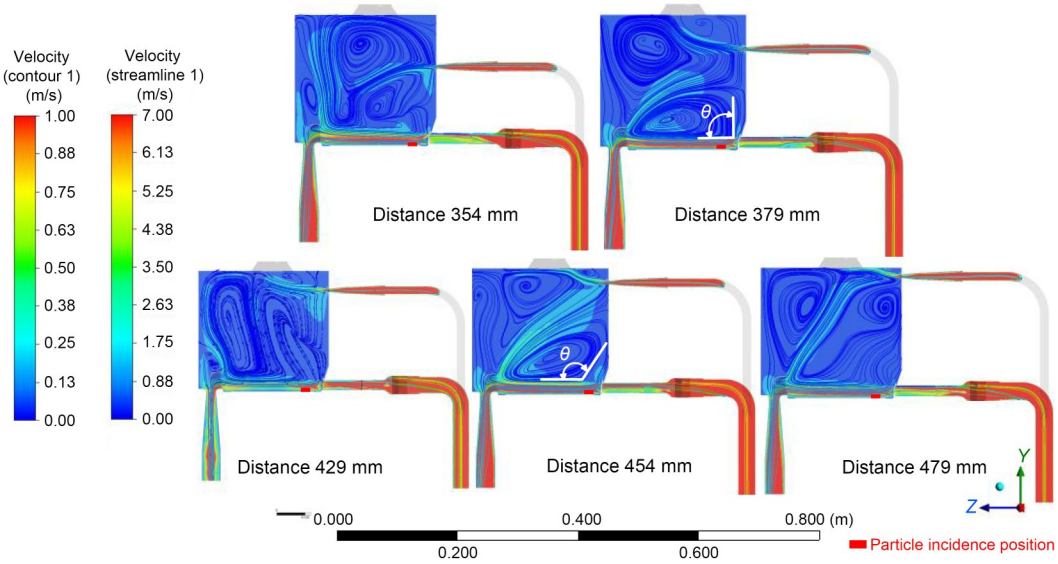

Fig. 6 Comparison of gas streamline diagrams for different positions of the second inlet (A–A′ plane)

(2) For the distance of 429 mm, the core of the clockwise-rotating vortex above the powder bed moved to the left of the build chamber. The downwash flow on the right of the clockwise-rotating vortex blew to the particle incidence position with an acute angle of θ. The acute angle of θ exerted a negative effect on the acceleration and homogeneity of laminar flow above the powder bed. The maximum spatter distance of the particles in the horizontal direction was 71.5 mm and the average distance was 62.5 mm. The maximum spatter height in the vertical direction was 49.2 mm. The spatter-removal rate was reduced to 16.9 %.

(3) For the distance of 379 mm, the downwash flow on the right of the vortex flowed to the particle incidence position with an angle of approximately 90° due to the impact of the right sidewall. This flow angle of the downwash flow brought about additional resistance to the particles in the vertical direction. The maximum spatter height of the spatters was 33.5 mm. The average spatter distance was 82.4 mm in the horizontal direction, which indicated that the laminar flow above the powder bed could exert a relatively large horizontal drag on the particles. The spatter-removal rate was 18.5%.

It can be inferred from the above that augmentation of horizontal drag and reduction of vertical resistance may enhance spatter removal. The spatter height of the particles will increase with the increase of the angle θ. A relatively high angle θ means the downwash flow on the right of the vortex turns to the horizontal direction at the right of the particle incidence position. An increase in horizontal drag is caused by the flow, which enhances the horizontal travel distance of the spatter. The trajectories of the particles are confined within the region encompassed by the two inlets.

Ferrar et al. (2012) found that increasing the homogeneity of the laminar flow near the powder bed reduced part porosity and increased compressive strength. We calculated the flow homogeneity on four horizontal planes above the powder bed, using Eq. (9). The four planes were located at 1, 5, 10, and 50 mm above the powder bed. As shown in Fig. 7, flow homogeneity was greatly influenced by the distance between the two inlets. It reached maximum values in all four horizontal planes at a distance of 379 mm.

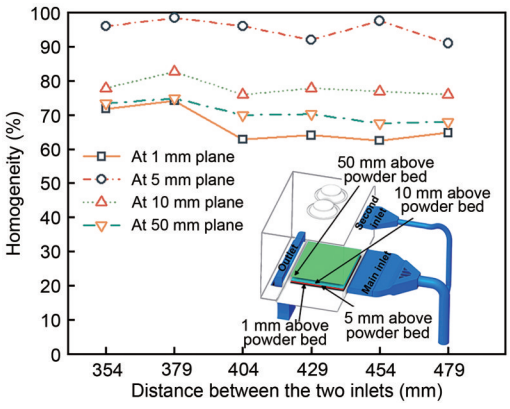

Fig. 7 Airflow homogeneity at different locations above the powder bed

A high spatter-removal rate is essential to attaining superior quality in parts manufacturing. Enhancing the velocity of the laminar flow can lead to an improvement in the removal rate (Zhang et al., 2020). The increase in flow homogeneity near the powder bed provided the possibility of raising the overall laminar flow velocity near the powder bed. This allowed greater flexibility in applying a larger pressure difference between the inlet and outlet. Meanwhile, it was necessary to consider the threshold velocity for powder particles jumping in the powder bed, to prevent the particles from "leapfrogging". Consequently, we chose a distance of 379 mm between the two inlets.

Analysis of the spatter trajectory showed that the trajectory was highly affected by the protective gas supplied by the second inlet. However, as shown in Fig. 2, the width of the powder bed and the spatter source in the X direction was 460 mm, while the width of the second inlet was only 250 mm. Thus, the second inlet could not cover the whole width of the powder bed. The spatter generated at both of the powder beds was weakly affected by the protective gas supplied by the second inlet. Fig. 8 presents the maximum spatter distance in the horizontal direction and the maximum spatter height in the vertical direction at different lateral positions in the X direction. The maximum spatter distances of the particles at the two sides of the powder bed were much shorter than those of the particles covered by the second inlet. Moreover, the maximum height of the particles at the two sides of the powder bed were much higher than those of the particles covered by the second inlet. The optimization of the second inlet was essential to improve the flow pattern at both sides of the powder bed.

We then tried a new type of inlet for the second inlet (Fig. 9). The width of the second inlet was increased to 500 mm, which was wider than the powder bed and the spatter source. Fig. 10 compares the streamlines of the build chamber with the original second inlet and the one with the modified second inlet. In the original design, the streamlines were concentrated in the middle of the build chamber, which meant that the protective gas supplied by the second inlet could not cover the entire powder bed well. The streamlines were evenly distributed in the build chamber with the modified second inlet. Fig. 11 shows the maximum spatter distance in the horizontal direction and the maximum spatter height in the vertical direction at different lateral positions in the X direction, for the build chamber with the modified second inlet. The homogeneity of the spatter trajectory clearly improved at each position in the powder bed. However, the modification of the second inlet increased the inlet width and airflow coverage area, which altered the pressure difference between the second inlet and the outlet. In

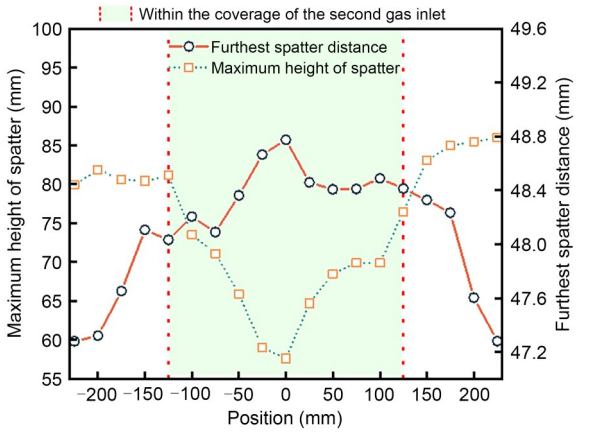

Fig. 8 Comparison of the particle paths along the width of the powder bed. References to color refer to the online version of this article

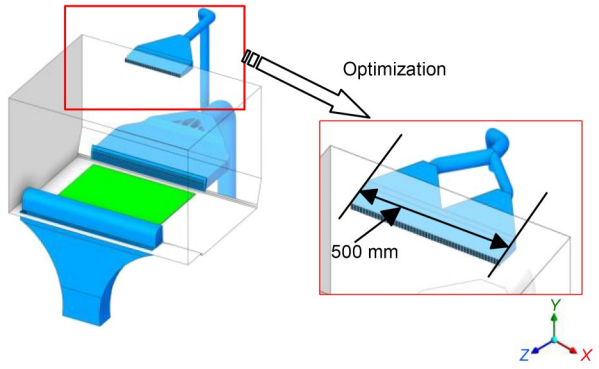

Fig. 9 Schematic of the modification of the second inlet

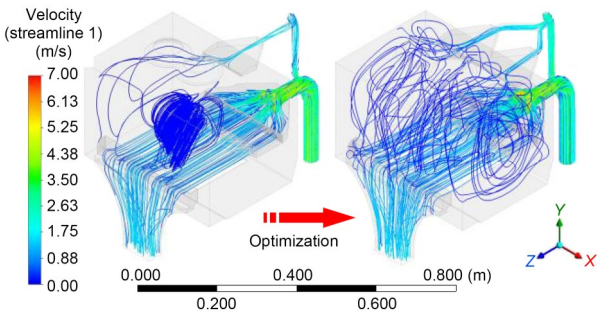

Fig. 10 Comparison of the streamlines in the build chamber with the original second inlet and the build chamber with the modified second inlet

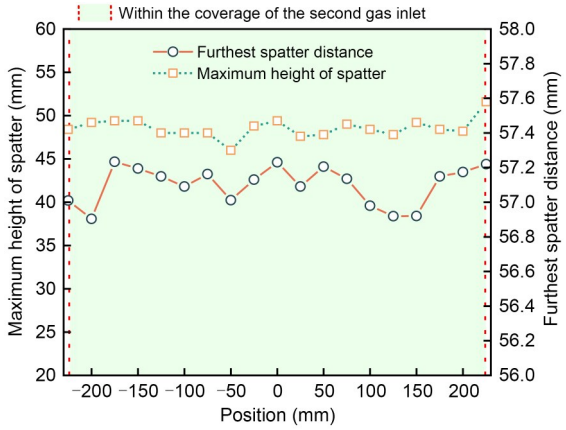

Fig. 11 Comparison of particle paths along the width of the powder bed for the build chamber with the modified second inlet. References to color refer to the online version of this article

spite of the improvement in flow homogeneity, the spatter-removal rate decreased slightly to 14.3%.

3.3 Anti-Coandaeffect design

The Coanda effect is also known as the wall-attachment effect. It describes the phenomenon of fluid flowing along the curvature of a wall if the curvature is small, due to fluid viscosity, rather than continuing in a straight line. Section 3.2 analyzes the effect of vortex-rotation direction on spatter trajectories. A more uniform flow past the powder bed was obtained with a distance of 379 mm for both inlets. In addition, insufficient coverage was solved by optimizing the second gas inlet, which enhanced the homogeneity of the influence of the protective gas on the spatter trajectory. However, the Coanda effect caused the downwash flow of the vortex to blow simulating the particle-injection point from the top down. This phenomenon limited particle spatter height. After a 90° turn to the powder bed, the horizontal flow became faster and more uniform. This resulted in spatter with a greater drag force and a longer spatter distance in the horizontal direction.

We employed the strategy of moving the right sidewall outwards (Fig. 12) to reduce the effect of the downwash flow induced by the Coanda effect above the particle-injection point. Fig. 12a shows the maximum spatter heights and removal rates of the particles with different moving distances. The maximum spatter height of the particles and the removal rate increased as the sidewall moved outwards in the range of 0 to 20 mm. The maximum values of the two

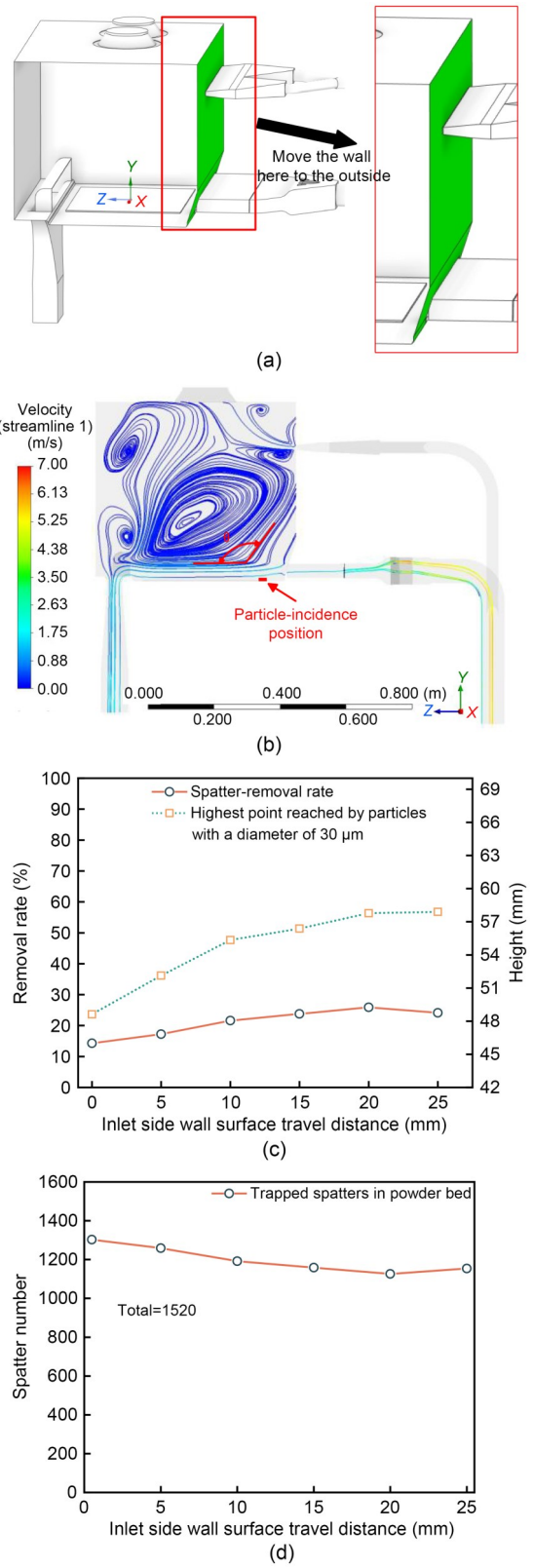

Fig. 12 Anti-Coanda effect design: (a) optimized design solution infographic; (b) center-plane (A–A′ plane) flow diagrams; (c) comparison of different inlet system designs; (d) number of trapped spatters in powder bed

parameters were obtained as the distance of the wall outward-moving reached 20 mm. As shown in Fig. 12c, the downwash flow on the right of the vortex flowed to the particle incidence position at the angle of the θ, which was greater than 90°. The change of downwash flow direction is beneficial because it increases the maximum spatter heights. However, an improvement in the removal rate is not evident compared with the increase in the maximum spatter height of the particles. Such a θ angle cannot provide sufficient horizontal drag force to the particles.

To address this issue, we propose a modified wall design, illustrated in Fig. 13. This design aims to alter the flow direction to augment the horizontal drag force acting on the particles. As shown in Fig. 13b, the downwash flow of the vortex above the powder bed is directed to turn along the sidewall on the right side of the particle incidence position. The downwash flow then blows to the particle incidence position from the right side. The change of the flow pattern around the particle incidence position reduces its influence on particle spatter height and brings sufficient horizontal drag to the particles. The removal rate can thus be increased to 47.5%.

The above discussion underscores the importance of maintaining the high velocity of the laminar flow above the powder bed in enhancing the spatter-removal rate. The pressure difference between the inlet and outlet is another important factor that affects the velocity of the laminar flow. Fig. 13c compares the removal rate and maximum velocity at the plane 1 mm above the powder bed when the inlet pressure is changed. Both parameters increased along with the inlet pressure. As the inlet pressure increased to 17.5 Pa (the corresponding flow rate is 1425.6 L/min), the maximum velocity overshot the threshold velocity. An inlet pressure of 15 Pa (the corresponding flow rate is 1349.5 L/min) is recommended. The spatter-removal rate increased to 76.1%, while the number of particles re-deposited onto the powder bed significantly decreased.

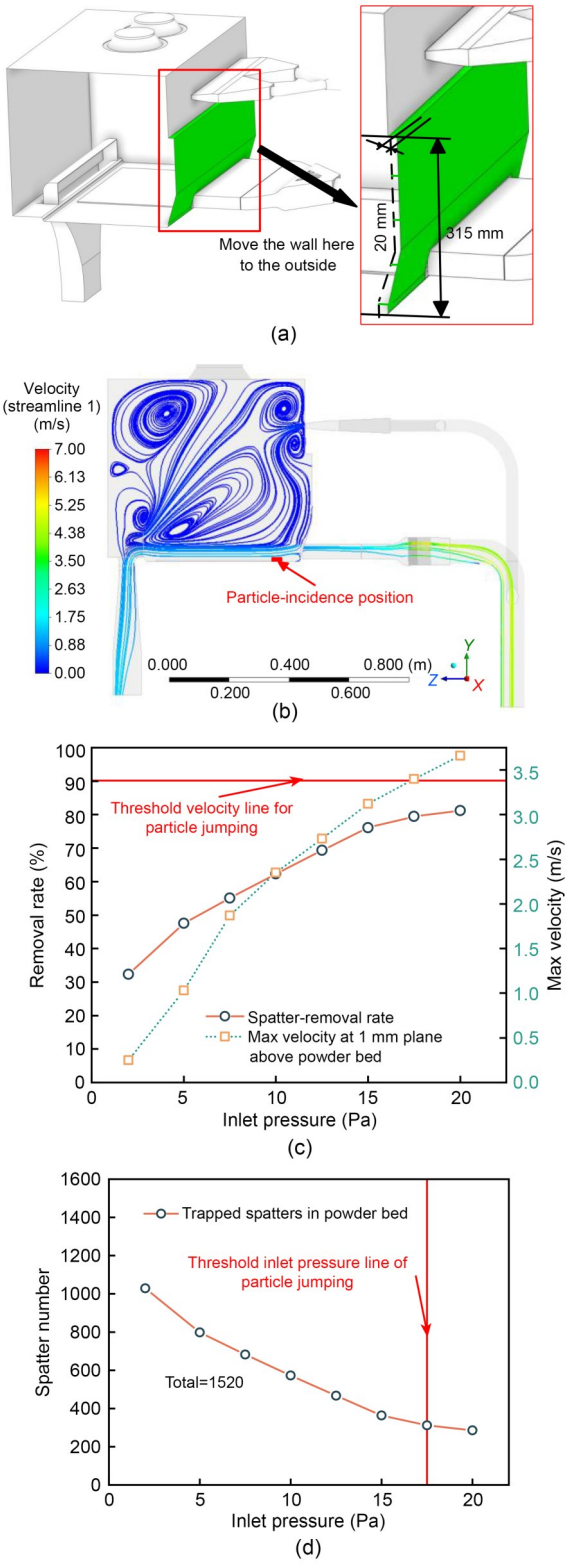

Fig. 13 Optimized anti-Coandaeffect design: (a) improved optimized design solution infographic; (b) center-plane (A–A′ plane) flow diagrams; (c) comparison of different inlet pressure designs; (d) number of trapped spatters in powder bed

4 Conclusions

We propose a novel gas-intake system with dual gas inlets to improve the flow field of the build chamber for L-PBF and reduce spatter during additive manufacturing. The gas-intake system with dual gas

inlets is optimized by adopting CFD technology. We developed a fully integrated CFD-DPM to simulate the interaction between spatter and gas flow. The gas flow around the powder bed and the spatter trajectories were carefully examined. The homogeneity and maximum velocity of the flow around the powder bed, and the spatter-removal, were used as the optimization criteria. Some conclusions can be drawn:

1. The addition of a second gas inlet greatly alters the flow structure in the L-PBF build chamber. The clockwise-rotating vortex occupies nearly the entire build chamber and is replaced by pairs of counter-rotating vortices, which suppresses the nose-up of the laminar flow passing the powder bed. A more uniform laminar flow is thus formed around the powder bed. The uniform laminar flow gives uniform drag to the spatter, which increases the removal rate of the spatter from 8.9% to 24.1%.

2. The distance between the main inlet and the second inlet plays an important role in the homogeneity of the laminar flow passing the powder bed. Reducing the distance between the two inlets results in a more uniform distribution of the laminar flow. The optimal distance between the two inlets is 379 mm.

3. The width of the second inlet is another key factor that affects the homogeneity of the laminar flow along the width of the powder bed. A narrow second inlet is insufficient to cover all the particles, which leads to high spatter height in the vertical direction at both width-wise sides of the powder bed. Increasing the width of the second inlet clearly improves the homogeneity of the flow and the spatter trajectory. However, this modification of the second inlet increases the flow area, which alters the pressure difference between the second inlet and the outlet. Thus, despite the improvement of flow homogeneity, the spatter-removal rate slightly decreases to 14.3%.

4. The Coanda effect along the right-side wall causes the downwash flow of the vortex to blow the simulated particle-injection point from the top down, which limits particle spatter height. Moving the lower half of the right-side wall outwards alters the direction of the flow blowing to the particle-injection point. This increases the removal rate to 47.5%. The pressure difference between the inlet and outlet also strongly affects the velocity of the laminar flow. Increasing the pressure difference improves the removal rate. Based on the threshold velocity, an inlet pressure of 15 Pa is recommended as the outlet pressure is −15 Pa (the corresponding flow rate is 1349.5 L/min). A removal rate of 76.1% can be obtained with this pressure difference.

Acknowledgments

This work is supported by the Natural Science Foundation of Jiangxi Province (Nos. 20224BAB214061 and 20224ACB214008), the National Natural Science Foundation of China (Nos. 52165043 and 52166002), the Jiangxi Provincial Cultivation Program for Academic and Technical Leaders of Major Subjects (No. 20225BCJ23008), the Anhui Provincial Natural Science Foundation (No. 2308085ME171), and the University Synergy Innovation Program of Anhui Province (Nos. GXXT-2023-025 and GXXT-2023-026), China.

Author contributions

Xin TIAN: conceptualization, software, methodology, and writing–original draft. Junwei ZHONG: data curation, funding acquisition, and writing–review & editing. Youwen YANG: writing–review & editing, and funding acquisition. Chaolei ZHANG: writing–review & editing, visualization, and validation. Long ZHAO: resources, software, and data curation.

Conflict of interest

Xin TIAN, Junwei ZHONG, Youwen YANG, Chaolei ZHANG, and Long ZHAO declare that they have no conflict of interest.

References

Amiri M, Payton EJ, 2021. An analytical model for prediction of denudation zone width in laser powder bed fusion additive manufacturing. *Additive Manufacturing*, 48:102461. https://doi.org/10.1016/j.addma.2021.102461

Andani MT, Dehghani R, Karamooz-Ravari MR, et al., 2018. A study on the effect of energy input on spatter particles creation during selective laser melting process. *Additive Manufacturing*, 20:33-43. https://doi.org/10.1016/j.addma.2017.12.009

Annovazzi A, Dembinski L, Blanchet E, et al., 2022. Influence of residual pressure on the melting of a powder bed induced by a laser beam. *Journal of Manufacturing Processes*, 73:715-724. https://doi.org/10.1016/j.jmapro.2021.11.007

Bin Anwar A, Pham QC, 2017. Selective laser melting of AlSi10Mg: effects of scan direction, part placement and inert gas flow velocity on tensile strength. *Journal of Materials Processing Technology*, 240:388-396. https://doi.org/10.1016/j.jmatprotec.2016.10.015

Bin Anwar A, Pham QC, 2018. Study of the spatter distribution on the powder bed during selective laser melting. *Additive Manufacturing*, 22:86-97. https://doi.org/10.1016/j.addma.2018.04.036

Bin Anwar A, Ibrahim IH, Pham QC, 2019. Spatter transport

by inert gas flow in selective laser melting: a simulation study. *Powder Technology*, 352:103-116. https://doi.org/10.1016/j.powtec.2019.04.044

Chien CY, Le TN, Lin ZH, et al., 2021. Numerical and experimental investigation into gas flow field and spattering phenomena in laser powder bed fusion processing of Inconel 718. *Materials & Design*, 210:110107. https://doi.org/10.1016/j.matdes.2021.110107

Constantin L, Kraiem N, Wu ZP, et al., 2021. Manufacturing of complex diamond-based composite structures via laser powder-bed fusion. *Additive Manufacturing*, 40:101927. https://doi.org/10.1016/j.addma.2021.101927

Debroy T, Mukherjee T, Wei HL, et al., 2021. Metallurgy, mechanistic models and machine learning in metal printing. *Nature Reviews Materials*, 6(1):48-68. https://doi.org/10.1038/s41578-020-00236-1

Dong Z, Han CJ, Zhao YZ, et al., 2024. Role of heterogenous microstructure and deformation behavior in achieving superior strength-ductility synergy in zinc fabricated via laser powder bed fusion. *International Journal of Extreme Manufacturing*, 6(4):045003. https://doi.org/10.1088/2631-7990/ad3929

Ferrar B, Mullen L, Jones E, et al., 2012. Gas flow effects on selective laser melting (SLM) manufacturing performance. *Journal of Materials Processing Technology*, 212(2):355-364. https://doi.org/10.1016/j.jmatprotec.2011.09.020

Gao Y, Zhang CL, Liu JL, et al., 2023. Optimizing the performance of wind field circulating track in laser powder bed fusion additive manufacturing. *The International Journal of Advanced Manufacturing Technology*, 124(11-12): 3963-3972. https://doi.org/10.1007/s00170-021-08060-9

Greses J, Hilton PA, Barlow CY, et al., 2004. Plume attenuation under high power Nd:yttritium–aluminum–garnet laser welding. *Journal of Laser Applications*, 16(1):9-15. https://doi.org/10.2351/1.1642636

Gunenthiram V, Peyre P, Schneider M, et al., 2018. Experimental analysis of spatter generation and melt-pool behavior during the powder bed laser beam melting process. *Journal of Materials Processing Technology*, 251: 376-386. https://doi.org/10.1016/j.jmatprotec.2017.08.012

Guo QL, Zhao C, Escano LI, et al., 2018. Transient dynamics of powder spattering in laser powder bed fusion additive manufacturing process revealed by in-situ high-speed high-energy X-ray imaging. *Acta Materialia*, 151:169-180. https://doi.org/10.1016/j.actamat.2018.03.036

Jadhav A, Jadhav VS, 2022. A review on 3D printing: an additive manufacturing technology. *Materials Today: Proceedings*, 62:2094-2099. https://doi.org/10.1016/j.matpr.2022.02.558

Kok JF, Parteli EJR, Michaels TI, et al., 2012. The physics of wind-blown sand and dust. *Reports on Progress in Physics*, 75(10):106901. https://doi.org/10.1088/0034-4885/75/10/106901

Ladewig A, Schlick G, Fisser M, et al., 2016. Influence of the shielding gas flow on the removal of process by-products in the selective laser melting process. *Additive Manufacturing*, 10:1-9. https://doi.org/10.1016/j.addma.2016.01.004

Matthews MJ, Guss G, Khairallah SA, et al., 2016. Denudation of metal powder layers in laser powder bed fusion processes. *Acta Materialia*, 114:33-42. https://doi.org/10.1016/j.actamat.2016.05.017

Nguyen HD, Sedao X, Mauclair C, et al., 2020. Non-diffractive Bessel beams for ultrafast laser scanning platform and proof-of-concept side-wall polishing of additively manufactured parts. *Micromachines*, 11(11):974. https://doi.org/10.3390/mi11110974

Pauzon C, Hoppe B, Pichler T, et al., 2021. Reduction of incandescent spatter with helium addition to the process gas during laser powder bed fusion of Ti-6Al-4V. *CIRP Journal of Manufacturing Science and Technology*, 35:371-378. https://doi.org/10.1016/j.cirpj.2021.07.004

Shao YP, Lu H, 2000. A simple expression for wind erosion threshold friction velocity. *Journal of Geophysical Research: Atmospheres*, 105(D17):22437-22443. https://doi.org/10.1029/2000JD900304

Shcheglov PY, Gumenyuk AV, Gornushkin IB, et al., 2013. Vapor-plasma plume investigation during high-power fiber laser welding. *Laser Physics*, 23(1):016001. https://doi.org/10.1088/1054-660x/23/1/016001

Simonelli M, Tuck C, Aboulkhair NT, et al., 2015. A study on the laser spatter and the oxidation reactions during selective laser melting of 316L stainless steel, Al-Si10-Mg, and Ti-6Al-4V. *Metallurgical and Materials Transactions A*, 46(9):3842-3851. https://doi.org/10.1007/s11661-015-2882-8

Sow MC, de Terris T, Castelnau O, et al., 2020. Influence of beam diameter on laser powder bed fusion (L-PBF) process. *Additive Manufacturing*, 36:101532. https://doi.org/10.1016/j.addma.2020.101532

Tan JH, Wong WLE, Dalgarno KW, 2017. An overview of powder granulometry on feedstock and part performance in the selective laser melting process. *Additive Manufacturing*, 18:228-255. https://doi.org/10.1016/j.addma.2017.10.011

Wang D, Wu SB, Fu F, et al., 2017. Mechanisms and characteristics of spatter generation in SLM processing and its effect on the properties. *Materials & Design*, 117:121-130. https://doi.org/10.1016/j.matdes.2016.12.060

Wang JY, Zhu YW, Li H, et al., 2022. Numerical study of the flow field and spatter particles in laser-based powder bed fusion manufacturing. *International Journal of Precision Engineering and Manufacturing-Green Technology*, 9(4): 1009-1020. https://doi.org/10.1007/s40684-021-00357-0

Yadroitsev I, Gusarov A, Yadroitsava I, et al., 2010. Single track formation in selective laser melting of metal powders. *Journal of Materials Processing Technology*, 210(12):

1624-1631.
https://doi.org/10.1016/j.jmatprotec.2010.05.010

Young ZA, Guo QL, Parab ND, et al., 2020. Types of spatter and their features and formation mechanisms in laser powder bed fusion additive manufacturing process. *Additive Manufacturing*, 36:101438.
https://doi.org/10.1016/j.addma.2020.101438

Zhang XB, Cheng B, Tuffile C, 2020. Simulation study of the spatter removal process and optimization design of gas flow system in laser powder bed fusion. *Additive Manufacturing*, 32:101049.
https://doi.org/10.1016/j.addma.2020.101049